


Interferometric pattern of the relativistic images of a Schwarzschild star

Yuan-Xing Gao (高原兴)¹ and Yi Xie (谢懿)^{2,*}

¹*School of Astronomy and Space Science, Nanjing University, Nanjing 210023, China*

²*Purple Mountain Observatory, Chinese Academy of Sciences, Nanjing 210023, China*

 (Received 2 November 2023; accepted 5 March 2024; published 26 March 2024)

For a horizonless Schwarzschild star with a photon sphere, its strong deflection gravitational lensing can generate unique inner relativistic images of pointlike sources, which are absent for a Schwarzschild black hole. In order to understand the signatures of its outer and inner relativistic images, we generalize the strong deflection limit method for an ultracompact object by including the finite distance effect of a source, and analytically calculate the complex visibility of all the relativistic images of the Schwarzschild star. We show that the interferometric pattern of the relativistic images of the Schwarzschild star has richer features than the one of the Schwarzschild black hole and is more likely to be resolved by future space-borne very long baseline interferometry.

DOI: [10.1103/PhysRevD.109.063030](https://doi.org/10.1103/PhysRevD.109.063030)

I. INTRODUCTION

Detection of gravitational waves from merging binary black holes [1–6] and direct images the supermassive black holes M87* [7–12] and Sgr A* [13–18], not only demonstrate the abundance of black holes in the Universe, but also offer new opportunities for exploring the laws of physics in the strong gravitational fields. A black hole with an event horizon and a central singularity is a fundamental object in Einstein’s general relativity. However, the presence of the event horizon blocks the connection between the interior and exterior regions of the black hole, resulting in Hawking radiation and the information paradox [19,20], while the singularity straightforwardly causes breakdown of general relativity. In pursuit of addressing these issues, the idea of black hole mimickers has been put forth in the literature (see Ref. [21] for a review). One prominent example is the simplest Schwarzschild interior solution, which removes the intrinsic singularity and event horizon of the Schwarzschild metric by introducing a bounded isotropic fluid into a region with a radius R slightly larger than the Schwarzschild radius R_s [22,23].

Besides being an exact solution of general relativity, the Schwarzschild interior solution is one of the few analytical solutions that can smoothly match the external Schwarzschild metric [24]. Such a solution characterizes an isotropic self-gravitating object with a uniform energy density, also known as a Schwarzschild star. It can be divided into two distinct classes. The first one is the Schwarzschild star with $R > 9R_s/8$ and positive internal pressure, and the second one is the supercompact Schwarzschild star with

$R < 9R_s/8$ and negative internal pressure [25,26]. It is demonstrated that both classes could maintain the radial stability [27]. The Schwarzschild star with $R = 9R_s/8$ shows a divergence in its pressure [28]. This critical radius comes from Buchdahl’s theorem, which states that any spherically symmetric object composed of isotropic fluids has an upper limit of its mass as $4c^2R/(9G)$ under the condition that the energy density is positive and monotonically decreases in the radial direction [28]. Although the Schwarzschild star suffers from the Buchdahl limit and its oversimplified uniform matter distribution, it has still attracted great attention, such as its anisotropy [29,30] and time dependence [31], and its connection to the gravastar [32,33]. These studies have also shed light on remarkable features of the Schwarzschild star, that the supercompact one with $R < 9R_s/8$ might have a nonvanishing positive tidal Love number [34] and a power-law tail very similar to the Schwarzschild black hole in the gravitational wave ringdown waveform [35].

The unique properties of the Schwarzschild star arouse the interest of identifying it observationally. It is feasible in principle to detect its lower multipoles or trailing echoes through gravitational waves, but this approach requires a high signal-to-noise ratio and thus challenges current technologies [35,36]. Searching for the Schwarzschild star can also be accomplished by electromagnetic wave observations [21]. Noteworthy discoveries achieved by the Event Horizon Telescope in recent years, such as shadows of M87* and Sgr A* [7,13] and characteristics of the accretion disk, highlight the significance of very long baseline interferometry in both astronomy and black hole physics. In extreme astrophysical environments near a compact object, electromagnetic emission of the accretion disk may be strongly deflected or even wind several times

*yixie@pmo.ac.cn

around the central compact object before reaching the observer. This phenomenon, often called the strong deflection gravitational lensing [37–51], results in the observed thick ring appearance of the accretion disk [7,13,52–56]. Enclosed within the ring are finer substructures, such as photon rings [57] and relativistic images [58]. The photon rings are formed by the emission winding around the gravitational lens [57,59]. Although the lower-order photon rings that are most easily accessible could be measured via future observations with the Earth-Moon baseline [60,61], they moderately depend on both the gravitational model of the compact object and the accretion physics [55,56]. In contrast, the relativistic images originate from the strong bending of the emission from small compact sources in the vicinity of the lens [50,58,62–65] and are thus independent of the accretion disk models, providing a more concise way to study the strong gravitational field around the compact object.

For a compact object with a photon sphere that is an unstable circular orbit for photons, we focus on the photons that have radial turning points in their trajectories, that are initially emitted in the radially inward direction by the sources outside the photon sphere, and that finally reach asymptotic observers. For the Schwarzschild black hole, these photons result in the formation of the outer relativistic images, the interferometric pattern of which can exhibit qualitatively similar staircaselike structures to those of the photon rings [58,60,66]. Taking Sgr A* as the lens, it is recently shown that the outermost image could be detected by an Earth-Moon baseline interferometry [58]. Inspired by these works, we will investigate the interferometric pattern of the relativistic images around a Schwarzschild star. Unlike the Schwarzschild black hole, the Schwarzschild star can have unique relativistic images inside the photon sphere. The outer and inner relativistic images make the interferometric pattern much more complicated, possibly helpful for distinguishing the Schwarzschild star from the Schwarzschild black hole. There are other types of photons' orbits, such as those trajectories outwardly beginning from a source inside the photon sphere, which might also generate relativistic images [67–69]. We leave these scenarios for our future work.

This paper is organized as follows. In Sec. II, we briefly review the metric of the Schwarzschild star, the geodesics of a photon and its special circular orbits, such as the photon and antiphoton spheres. In Sec. III, analytical approaches to describe the relativistic images of a pointlike source are given. Considering the finite distance of a source, we generalize the strong deflection limit method for the relativistic images inside the photon sphere [64]. In Sec. IV, we calculate the interferometric pattern of all the relativistic images of the Schwarzschild star and study the features in this pattern. In Sec. V, we explore how to infer the properties of a spacetime from those observables. We conclude and discuss our results in Sec. VI.

II. SCHWARZSCHILD STAR

A. Metric

The Schwarzschild star, or the Schwarzschild interior solution, describes a static spherically symmetric object with a uniform energy density. Its line element reads ($G = c = 1$) [22,23]

$$ds^2 = -A(r)dt^2 + B(r)dr^2 + C(r)(d\theta^2 + \sin^2\theta d\phi^2), \quad (1)$$

with

$$A(r) = \begin{cases} \left(\frac{3}{2}\sqrt{\mathcal{H}_R} - \frac{1}{2}\sqrt{\mathcal{H}_r}\right)^2, & r < R \\ 1 - \frac{R_s}{r}, & r \geq R \end{cases}, \quad (2)$$

$$B(r) = \begin{cases} \mathcal{H}_r^{-1}, & r < R \\ \left(1 - \frac{R_s}{r}\right)^{-1}, & r \geq R \end{cases}, \quad (3)$$

$$C(r) = r^2, \quad (4)$$

where the hypersurface $r = R$ connects the internal and external spacetime, $R_s = 2M$ is the Schwarzschild radius, M is the Arnowitt-Deser-Misner mass, and \mathcal{H}_R and \mathcal{H}_r are respectively defined as

$$\mathcal{H}_R = 1 - \frac{1}{\zeta}, \quad (5)$$

$$\mathcal{H}_r = 1 - \frac{r^2}{\zeta R^2}, \quad (6)$$

with ζ being the normalized radius as

$$\zeta = \frac{R}{R_s}. \quad (7)$$

The Schwarzschild star gets more compact as ζ decreases. It is easy to find that the metric (1) does not have an event horizon since $\zeta > 1$ and the inverse of $B(r)$ is always positive.

The pressure of the incompressible isotropic fluid $\text{diag}(\bar{\epsilon}, p, p, p)$ that makes up the Schwarzschild star is given by [26]

$$p(r) = \bar{\epsilon} \left(\frac{\sqrt{\mathcal{H}_r} - \sqrt{\mathcal{H}_R}}{3\sqrt{\mathcal{H}_R} - \sqrt{\mathcal{H}_r}} \right), \quad (8)$$

with $\bar{\epsilon}$ being the constant energy density as

$$\bar{\epsilon} = \begin{cases} \frac{3}{8\pi\zeta R^2} = \text{const}, & r < R \\ 0, & r \geq R \end{cases}. \quad (9)$$

From the metric (1) and the pressure (8), $p(r)$ diverges when $A(R_0) = 0$, in which R_0 locates at [26]

$$R_0 = 3\zeta\sqrt{1 - \frac{8}{9}\zeta R_s}. \quad (10)$$

In the Buchdahl limit [28], we can have

$$\zeta_B = \frac{9}{8}. \quad (11)$$

For $\zeta = \zeta_B$, Eq. (10) gives $R_0 = 0$ and the central pressure $p(0)$ diverges from Eq. (8). In this case, the Schwarzschild star is unstable since it is hard to keep the state of hydrostatic equilibrium, triggering a gravitational collapse to form a Schwarzschild black hole [26–28]. For $\zeta > \zeta_B$, Buchdahl's theorem is satisfied. $A(r)$ is always positive and its root R_0 is imaginary, and $p(r)$ is thus positive and regular everywhere. For $\zeta < \zeta_B$, Buchdahl's theorem is broken. $A(r)$ is positive except at R_0 , and R_0 is real and belongs to $(0, R)$. In this situation, $p(r)$ is negative, divergent and positive at $0 < r < R_0$, $r = R_0$ and $r > R_0$, respectively. The Schwarzschild star with $\zeta < \zeta_B$ is called the supercompact Schwarzschild star [26]. In the case of $R \rightarrow R_s^+$ (or equivalently $\zeta \rightarrow 1^+$) and $R_0 \rightarrow R_s^-$, the interior region of the supercompact Schwarzschild star becomes a modified de Sitter core with constant negative pressure and can match the exterior metric as required by the Israel junction conditions [27,35], providing a gravastar explanation for the Schwarzschild star [32,33]. In such an extreme context, it is shown that the interior is regular at $r = 0$, and $p(r)$ diverges exactly at $r = R$ but can be regularized through the Komar formula [25,27].

B. Geodesic motion of photon

In the Schwarzschild star spacetime, a photon has two constants of motion, i.e., the energy and angular momentum, given by

$$E = A(r)\dot{t}, \quad (12)$$

$$L = C(r)\dot{\phi}. \quad (13)$$

These two quantities are related to the impact parameter u with

$$u \equiv \frac{L}{E}. \quad (14)$$

The photon travels along a geodesic with the following equation of motion

$$A(r)B(r)\dot{r}^2 + L^2V_{\text{eff}} = E^2. \quad (15)$$

The effective potential per L^2 is defined as

$$V_{\text{eff}} = \frac{A(r)}{C(r)}. \quad (16)$$

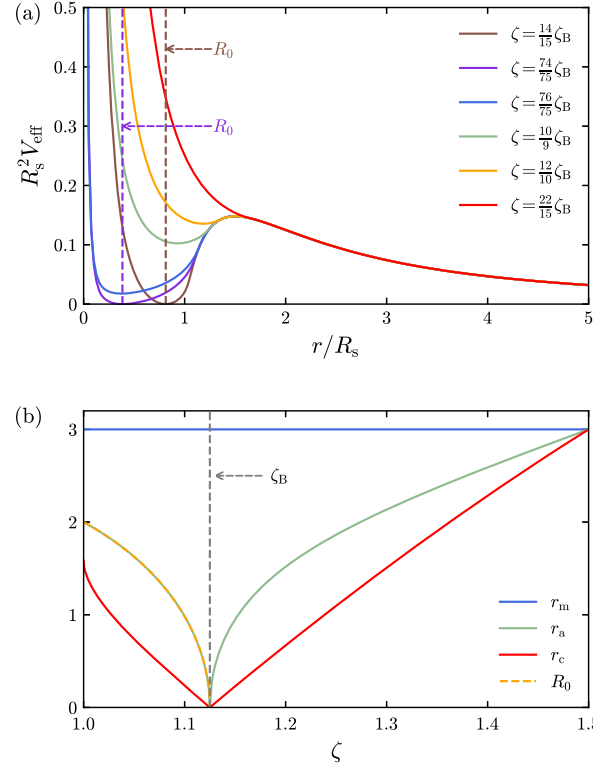


FIG. 1. (a) The effective potential V_{eff} with respect to the radial coordinates r for several normalized radii ζ . (b) The positions of the photon sphere r_m , the antiphoton sphere r_a and the point of r_c with respect to ζ .

Figure 1(a) shows the effective potential V_{eff} with respect to the radial coordinate r for several values of the normalized radius ζ . It shows that the minimum of V_{eff} approaches 0 when $\zeta \rightarrow 1$. As ζ increases, the maximum and minimum of V_{eff} get closer to each other, and finally merge when ζ reaches 1.5. As shown in Fig. 1(a), R_0 exists only if $\zeta < \zeta_B$ and it coincides with the location of the minimum of V_{eff} .

In this work, we consider the photons with the following conditions:

- (i) their trajectories have radial turning points r_0 ;
- (ii) they are emitted by the sources located outside the photon sphere, i.e. $r_s > r_m$, where r_s and r_m are the radial coordinate of the source and the radius of the photon sphere, respectively;
- (iii) they are initially emitted in the radially inward direction, $\dot{r} < 0$;
- (iv) they can finally reach asymptotic observers''.

With $\dot{r} = 0$ and $L^2V_{\text{eff}}(r_0) = E^2$ at the turning point r_0 , we can have the relation between r_0 and the impact parameter u as

$$u = \sqrt{\frac{C(r_0)}{A(r_0)}}. \quad (17)$$

A positive and finite impact parameter u demands $r_0 > R_0$ since $A(R_0) = 0$ directly causes u to diverge due to Eq. (17). For the photons satisfying the aforementioned conditions, they cannot enter the region $r_0 \leq R_0$. These photons' geodesic, Eq. (15), is ill defined since $\dot{r}(r = R_0)$ diverges. Meanwhile, the metric function $A(R_0) = 0$ indicates that $r = R_0$ would be an infinite redshift surface, so that an asymptotic observer cannot see the photons (initially emitted in the radially inward direction) passing through this surface. However, these issues hold only for the supercompact Schwarzschild star that breaks the Buchdahl's theorem and always has $R_0 \in (0, R)$, but is free for the Schwarzschild star with $\zeta > \zeta_B$ due to the fact that its $A(r)$ is positive when the Buchdahl's theorem is satisfied. In summary, one of the following two conditions must be met to ensure that a lensed photon could reach an observer: (1) $\zeta < \zeta_B$ and $r > R_0$; or (2) $\zeta > \zeta_B$.

Circular orbits play a vital role in the geodesic motion of photons near a compact object, which determine the characteristics in electromagnetic wave observation. The conditions for the photon circular orbits are given by $\dot{r} = 0$ and $V'_{\text{eff}}(r) = 0$, where the prime stands for the derivative with respect to the radial coordinate r . $V'_{\text{eff}}(r_m) = 0$ and $V''_{\text{eff}}(r_m) < 0$ define the unstable circular orbit of photons, i.e., the photon sphere. According to Appendix A, we find that if $\zeta < 1.5$, the Schwarzschild star has a photon sphere at

$$r_m = \frac{3}{2}R_s. \quad (18)$$

For $\zeta \geq 1.5$, no photon sphere exists for the Schwarzschild star. In the limit $r_0 \rightarrow r_m^+$, a photon will wind several times around the Schwarzschild star and then escape, forming relativistic images outside the photon sphere finally. Compared with the Schwarzschild black hole that has only one circular photon orbit, the ultracompact Schwarzschild star can have multiple photon and antiphoton spheres, see Refs. [70,71] for other interesting cases.

$V'_{\text{eff}}(r_a) = 0$ and $V''_{\text{eff}}(r_a) > 0$ define the stable circular orbit, i.e., the antiphoton sphere. A stable circular photon orbit might trigger nonlinear instabilities [72,73], causing an ultracompact object to evolve into a less compact one or a black hole [36]. We show that the antiphoton sphere r_a and R_0 share the same expression (10) (see Appendix A). For a photon emitted by a source located outside the photon sphere, it can only propagate in the region $r > r_a = R_0$ without an entrance to the region $r \leq r_a = R_0$. This suggests that the antiphoton sphere plays no role, and thus the strong deflection gravitational lensing by the supercompact Schwarzschild star with $\zeta < \zeta_B$ is still controlled by the photon sphere r_m whether its surface $R(> R_0)$ is electromagnetic transparent or not. Therefore, we expect that the supercompact Schwarzschild star may produce electromagnetic signals almost identical to those of the

Schwarzschild black hole. At this point, detection of its gravitational wave would be a better way to distinguish such a black hole mimicker [35].

In order to ensure that the Schwarzschild star has a photon sphere and has distinguishable features from the Schwarzschild black hole in the electromagnetic wave, we focus on the following parameter space of ζ

$$\mathcal{D} = \left\{ \zeta \mid \zeta_B < \zeta < \frac{3}{2} \right\}. \quad (19)$$

It makes a real R_0 vanish and an antiphoton sphere r_a exist at

$$r_a = \frac{\zeta^{3/2}}{3} \sqrt{\frac{8\zeta - 9}{\zeta - 1}} R_s < R. \quad (20)$$

Due to the presence of the antiphoton sphere, there is a $r_c < r_m$, which satisfies

$$\frac{A(r_c)}{C(r_c)} = \frac{A(r_m)}{C(r_m)}, \quad (21)$$

or $u(r_c) = u_m = u(r_m)$. For a Schwarzschild star, we can find

$$r_c = \frac{3\sqrt{3}\zeta}{16\zeta^3 + 27} Q(\zeta) R_s, \quad (22)$$

where

$$Q(\zeta) = 12\sqrt{\zeta^4 - \zeta^3} - \sqrt{16\zeta^4 - 216\zeta + 243}. \quad (23)$$

We show r_m , r_a and r_c with respect to ζ in Fig. 1(b). It also demonstrates that R_0 coincides with r_a for $\zeta < \zeta_B$. The presence of r_c leads to the fact that a photon with its impact parameter less than u_m may have its turning point r_0 inside the photon sphere. Therefore, a photon entering the photon sphere might escape from the interior, as long as the surface of the Schwarzschild star does not absorb it. Here, following Refs. [21,74], we assume that the Schwarzschild star does not emit electromagnetic waves itself and has an electromagnetically transparent surface with relatively high absorption rate in its interior, which satisfy currently observational constraints on M87* and Sgr A* from Event Horizon Telescope [12,18]. In the limit $r_0 \rightarrow r_c^-$, it was found that a light ray can also be strongly deflected to form a series of relativistic images inside the photon sphere [64], a phenomenon not generally found in black hole spacetime (see [70,71] for counterexamples).

For gravitational lensing in the spacetime (1), the change in the azimuthal angle of the photon satisfying the conditions (i)–(iv) can be obtained as [75]

$$\begin{aligned}\Delta\phi &= \sum_{i=S,O} \int_{r_0}^{r_i} \frac{\dot{\phi}}{r} dr \\ &= \sum_{i=S,O} \int_{r_0}^{r_i} \sqrt{\frac{C_0 A(r) B(r)}{C(r) [A_0 C(r) - A(r) C_0]}} dr, \quad (24)\end{aligned}$$

where the subscript “0” represents functions evaluated at r_0 , and r_S and r_O are the radial coordinates of the source and the observer, respectively. In general, r_O locates in the asymptotically flat region of the spacetime and thus we have $r_O \gg R_s$. For a photon that can be received by the observer, its source might be located anywhere as long as $r_S \geq r_0$. As $r_0 \rightarrow r_m^+$ or $r_0 \rightarrow r_m^-$, we reach the strong deflection limit of the gravitational lensing, which allows us to deal with the integral (24) analytically [63,64].

The relation among the source, the observer, the gravitational lens and images is described by the lens equation. Taking the gravitational lens as the origin of the coordinates, the lens equation in the strong deflection gravitational lensing reads [37]

$$\Delta\phi = \phi_O \mp \phi_S + 2n\pi, \quad (25)$$

where \mp accounts for images appearing on the same (−) or opposite side (+) of the source, n denotes the winding number, ϕ_S and ϕ_O stand for the azimuthal angle of the source and the observer, respectively. Without loss of generality, we set $\phi_O = \pi$ in the following parts of this work.

III. RELATIVISTIC IMAGES OF SCHWARZSCHILD STAR

A. Outer relativistic images

In the strong deflection limit $r_0 \rightarrow r_m^+$, a photon with impact parameter $u \rightarrow u_m^+$ will wind several times before being reception the observer and finally form an outer relativistic image outside the photon sphere. The change in the azimuthal angle (24) for this image can be analytically found as [58]

$$\begin{aligned}\Delta\phi &= -\bar{a}_+ \log \frac{\epsilon_+}{z_O z_S} + \bar{b}_+ + \pi \\ &+ \mathcal{O}[(u - u_m) \log(u - u_m)], \quad (26)\end{aligned}$$

where

$$\epsilon_+ = \frac{u}{u_m} - 1, \quad (27)$$

$$z_O = 1 - \frac{r_m}{r_O}, \quad z_S = 1 - \frac{r_m}{r_S}, \quad z = 1 - \frac{r_m}{r}, \quad (28)$$

$$\bar{a}_+ = \sqrt{\frac{2B_m A_m}{C_m'' A_m - C_m A_m''}}, \quad (29)$$

$$\begin{aligned}\bar{b}_+ &= -\pi + \bar{a}_+ \log \left[r_m^2 \left(\frac{C_m''}{C_m} - \frac{A_m''}{A_m} \right) \right] \\ &+ \left(\int_0^{z_O} + \int_0^{z_S} \right) g_1(z) dz, \quad (30)\end{aligned}$$

$$g_1(z) = \frac{r_m}{(1-z)^2} \sqrt{\frac{C_m A(z) B(z)}{[A_m C(z) - A(z) C_m] C(z)}} - \frac{\bar{a}_+}{|z|}. \quad (31)$$

The subscript “m” represents quantities evaluated at $r = r_m$. Both the Schwarzschild star and the Schwarzschild black hole have $\bar{a}_+ = 1$.

Combing the change in the azimuthal angle (26) with the lens equation (25), we can obtain [58]

$$\epsilon_{+n,\pm} = \frac{u_{+n,\pm}}{u_m} - 1 = z_O z_S e^{\frac{\bar{b}_+ \pm \phi_S - 2n\pi}{\bar{a}_+}}, \quad (32)$$

where the subscript “+n” denotes quantities of the n th-order outer relativistic images, and “±” accounts for the image appearing on the same (+, positive parity) or opposite (−, negative parity) side of the source. For an observer located in the asymptotically flat region, the angular separation between the image and the lens is $\vartheta = u/D_{OL}$. So we can have the angular position of the n th-order outer relativistic images as [58]

$$\vartheta_{+n,\pm} = \frac{u_m}{D_{OL}} (1 + \epsilon_{+n,\pm}) = \theta_\infty (1 + \epsilon_{+n,\pm}), \quad (33)$$

where θ_∞ is the apparent radius of the photon sphere. Moreover, the size of an image itself is also a vital observational characteristic. A relativistic image appears as an extremely thin tangentially elongated arc [76], and can be decomposed into the tangential length and the radial thickness. The tangential length of the source $\Delta\vartheta_S$ remains unchanged by gravitational lensing, which indicates that $\Delta\vartheta_{\text{image}} = \Delta\vartheta_S$ for different images, and for a spherical source we have $\Delta\vartheta_S = \Delta r_S / (r_S \sin \phi_S)$ [58]. The radial thickness of the n th-order outer images can be found by differentiating Eq. (33) as [58]

$$\Delta\vartheta_{+n,\pm} = \theta_\infty \Delta\epsilon_{+n,\pm} \quad (34)$$

where

$$\Delta\epsilon_{+n,\pm} = \left\{ \frac{\Delta\phi_S}{\bar{a}_+} + \frac{r_m}{r_S^2} \left[\frac{1}{z_S} + \frac{g_1(z_S)}{\bar{a}_+} \right] \Delta r_S \right\} \epsilon_{+n,\pm}. \quad (35)$$

To separate the contributions of the source and lens, we can rewrite Eq. (34) as [58]

$$\Delta\vartheta_{+n,\pm} = \Delta\vartheta_0 \epsilon_{+n,\pm}, \quad (36)$$

where $\Delta\vartheta_0$ is the geometric factor

$$\Delta\vartheta_0 = \frac{\theta_\infty}{\bar{a}_+} \Delta\phi_S + \theta_\infty \frac{r_m}{r_S^2} \left[\frac{1}{z_S} + \frac{g_1(z_S)}{\bar{a}_+} \right] \Delta r_S, \quad (37)$$

and it contains the source information such as its radial angular diameter Δr_S and its azimuthal angle diameter $\Delta\phi_S \approx \Delta r_S/r_S$.

B. Inner relativistic images

In the strong deflection limit $r_0 \rightarrow r_c^-$, a photon with $u \rightarrow u_m^-$ can enter the region inside the photon sphere, but unlike the Schwarzschild black hole, this photon may not be absorbed by the horizonless Schwarzschild star. With the presence of the antiphoton sphere, it is still possible for the photon to reach the observer after winding several times in the nearby region within the photon sphere, and eventually generate an inner relativistic image inside the photon sphere. In the context of a source at infinity, Ref. [64] proposed a method to calculate observables of the inner relativistic images. However, the source may be practically located in the vicinity of the gravitational lens, such as a hot cloud produced by the tidal disruption of a star [58]. Due to the absence of the source distance, larger relative errors in the strong deflection limit formula for its relativistic images may emerge. Therefore, we generalize the method proposed by Ref. [64] to account for the effect of finite source distance on gravitational lensing.

We find that $\Delta\phi$ in the strong deflection limit of $r_0 \rightarrow r_c^-$ is given by

$$\begin{aligned} \Delta\phi &= I_D + I_R \\ &= -\bar{a}_- \log \frac{\epsilon_-}{\sqrt{z_O z_S}} + \bar{b}_- + \pi \\ &\quad + \mathcal{O}[(u_m^2 - u^2) \log(u_m^2 - u^2)], \end{aligned} \quad (38)$$

where

$$\epsilon_- = \frac{u_m^2}{u^2} - 1, \quad (39)$$

$$\bar{a}_- = \frac{2r_m}{\sqrt{\eta_m}} = 2\bar{a}_+, \quad (40)$$

$$\begin{aligned} \bar{b}_- &= -\pi + 2\bar{a}_+ \log \left[2r_m^2 \left(\frac{C_m''}{C_m} - \frac{A_m''}{A_m} \right) \left(\frac{r_m}{r_c} - 1 \right) \right] \\ &\quad + \left(\int_{1-\frac{r_m}{r_c}}^{z_O} + \int_{1-\frac{r_m}{r_c}}^{z_S} \right) g_2(z) dz, \end{aligned} \quad (41)$$

$$g_2(z) = \frac{r_m}{(1-z)^2} \sqrt{\frac{C_c A(z) B(z)}{[A_c C(z) - A(z) C_c] C(z)}} - \frac{\bar{a}_+}{|z|}. \quad (42)$$

Its detailed derivation is give in Appendix B. From the definition (21) of r_c , we know

$$g_1(z) = g_2(z). \quad (43)$$

Due to the dependence of z_S and z_O , our result of Eq. (38) can more accurately approximate the change in the azimuthal angle of the photon propagating from the source at $r = r_S > r_m$ to the observer at $r = r_O > r_m$ than the one of Ref. [64]. In the limit $r_S, r_O \rightarrow \infty$ or $z_S, z_O \rightarrow 1$, Eq. (38) recovers the result in Ref. [64]. It can be used to study the finite distance effect of both the source and the observer on the strong deflection gravitational lensing near the anti-photon sphere.

For a Schwarzschild star with $\zeta = 5/4$, Fig. 2 illustrates relative errors of both our result of Eq. (38) and the formula of Ref. [64] with respect to numerical results for some sources with finite distances. It demonstrates that our result of Eq. (38) has smaller relative errors, basically below 1.5%, and is thus better when taking the finite distance effect into account. On the other hand, the interferometric

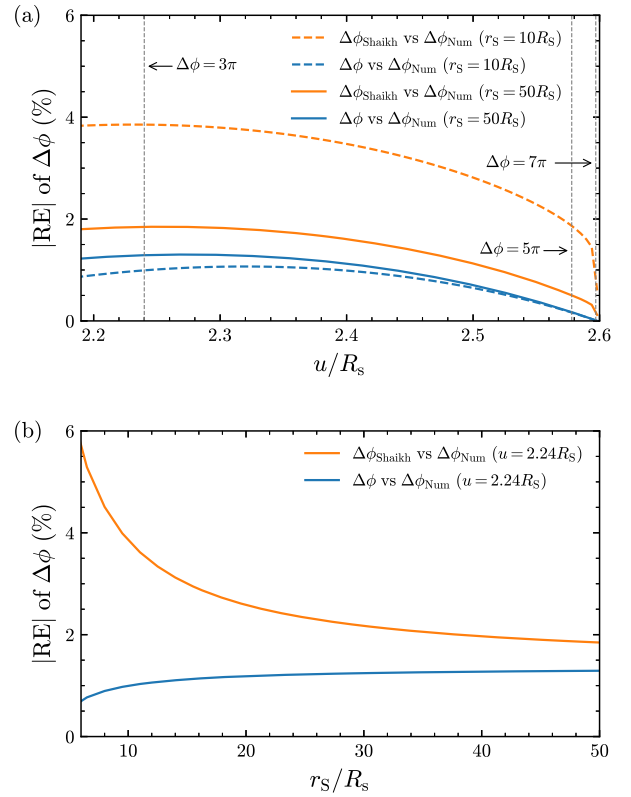


FIG. 2. (a) Relative errors of both our approximation (38) (blue lines) and the one in Ref. [64] (orange lines) with various impact parameters are shown by fixing the observer distance $r_O = 5 \times 10^5 R_s$ and considering the source distance either $r_S = 10R_s$ (dashed lines) or $r_S = 50R_s$ (solid lines). The three gray dotted lines from left to right represent respectively the impact parameters $u \approx 2.24R_s, 2.58R_s$ and $2.59R_s$, corresponding to $\Delta\phi = 3\pi, 5\pi$ and 7π without taking the finite distance effect into account. (b) Relative errors of our approximation (38) (blue lines) and of the one in Ref. [64] (orange lines) with respect to the source distance are shown by fixing $u = 2.24R_s$ and $\zeta = 5/4$.

signals of relativistic images can be significantly affected by the source characteristics, such as the intensity, shape and size [58]. To study the influence of these characteristics, it is important to introduce the finite distance effect. Therefore, we will use Eq. (38) to approximate the change in the azimuthal angle $\Delta\phi$ later.

For the inner relativistic images, the lens equation (25) still holds. Combining Eqs. (38) and (25), we can obtain

$$\epsilon_{-n,\pm} = \frac{u_m^2}{u_{-n,\pm}^2} - 1 = \sqrt{z_0 z_S} e^{\frac{\bar{b}_{-n,\pm} \phi_S - 2n\pi}{\bar{a}_-}}, \quad (44)$$

where “ $-n$ ” denotes the n th-order inner relativistic images, and the angular position of the n th-order inner relativistic images as

$$\begin{aligned} \vartheta_{-n,\pm} &= \frac{\theta_\infty}{\sqrt{1 + \epsilon_{-n,\pm}}} \\ &= \theta_\infty \left(1 - \frac{\epsilon_{-n,\pm}}{2} \right) + \mathcal{O}(\epsilon_{-n,\pm}^2). \end{aligned} \quad (45)$$

The radial thickness of the n th-order images inside the photon sphere can be derived by differentiating Eq. (45) as

$$\Delta\vartheta_{-n,\pm} = \Delta\vartheta'_0 \frac{\epsilon_{-n,\pm}}{(1 + \epsilon_{-n,\pm})^{3/2}} \quad (46)$$

$$= \Delta\vartheta'_0 \epsilon_{-n,\pm} + \mathcal{O}(\epsilon_{-n,\pm}^2), \quad (47)$$

where

$$\Delta\vartheta'_0 = \frac{\theta_\infty}{2} \frac{\Delta\phi_S}{\bar{a}_-} + \frac{\theta_\infty}{2} \frac{r_m}{r_S^2} \left[\frac{1}{2z_S} + \frac{g_2(z_S)}{\bar{a}_-} \right] \Delta r_S. \quad (48)$$

From Eqs. (37), (40), (43) and (48), we can have

$$\Delta\vartheta'_0 = \frac{1}{4} \Delta\vartheta_0. \quad (49)$$

Although $\Delta\vartheta'_0$ for the inner relativistic images is only a quarter of $\Delta\vartheta_0$ for the outer relativistic images, the magnitude of $\epsilon_{-n,\pm}$ is usually much larger than the one

of $\epsilon_{+n,\pm}$. Therefore, the radial thickness of the n th-order inner relativistic image is still larger than that of the n th-order outer one in most instances.

IV. INTERFEROMETRIC PATTERN OF RELATIVISTIC IMAGES

With the position and size of the inner and outer relativistic images, we will study the interferometric pattern of these images. In this section, we consider a static source that is far enough away from the lens. In this situation the misalignment caused by the time delay between different images can be negligible, i.e., all images lie on the same line [58]. When the source is sufficiently distant, the gravitational redshift effect can also be ignored, and all images share the same intensity I_0 . Denoting (x, y) as the celestial coordinates of the relativistic images, we follow Ref. [58] and assume that the inner and outer relativistic images has a Gaussian intensity distribution with the maximum locating at $(\vartheta_{\pm n,\pm}, 0)$, radial thickness $\Delta\vartheta_{\pm n,\pm}$ in the x direction and tangential length $\vartheta_{\pm n,\pm} \Delta\vartheta_S$ in the y direction. Then we can write the intensity distribution $I(x, y)$ for the inner and outer relativistic images as

$$\begin{aligned} I(x, y) &= I_0 \sum_{p=\pm} \sum_{n=1}^{+\infty} \left[e^{-\frac{(x-p\vartheta_{+n,p})^2}{2\Delta\vartheta_{+n,p}^2}} e^{-\frac{y^2}{2\vartheta_{+n,p}^2 \Delta\vartheta_S^2}} \right. \\ &\quad \left. + e^{-\frac{(x-p\vartheta_{-n,p})^2}{2\Delta\vartheta_{-n,p}^2}} e^{-\frac{y^2}{2\vartheta_{-n,p}^2 \Delta\vartheta_S^2}} \right]. \end{aligned} \quad (50)$$

Leaving aside the second term in the bracket of (50), we recover the case of the Schwarzschild black hole discussed in Ref. [58].

The two-dimensional Fourier transform of the intensity distribution $I(x, y)$ gives the complex visibility of the relativistic images [77]

$$\mathcal{V}(\mathbf{u}, \mathbf{v}) = \int \int I(x, y) e^{-j2\pi(\mathbf{u}x + \mathbf{v}y)} dx dy, \quad (51)$$

where (\mathbf{u}, \mathbf{v}) is the two-dimensional spatial frequency. With Eq. (50), we can obtain

$$\begin{aligned} \mathcal{V}(\mathbf{u}, \mathbf{v}) &= 2\pi I_0 \sum_{p=\pm} \sum_{n=1}^{+\infty} \Delta\vartheta_S [\vartheta_{+n,p} \Delta\vartheta_{+n,p} e^{-2\pi^2 \Delta\vartheta_{+n,p}^2 u^2 - j2\pi p \vartheta_{+n,p} u} e^{-2\pi^2 \vartheta_{+n,p}^2 \Delta\vartheta_S^2 v^2} \\ &\quad + \vartheta_{-n,p} \Delta\vartheta_{-n,p} e^{-2\pi^2 \Delta\vartheta_{-n,p}^2 u^2 - j2\pi p \vartheta_{-n,p} u} e^{-2\pi^2 \vartheta_{-n,p}^2 \Delta\vartheta_S^2 v^2}], \end{aligned} \quad (52)$$

where $\vartheta_{+n,\pm} \Delta\vartheta_{+n,\pm}$, $\vartheta_{+n,\pm} \Delta\vartheta_S$, $\vartheta_{-n,\pm} \Delta\vartheta_{-n,\pm}$ and $\vartheta_{-n,\pm} \Delta\vartheta_S$ depend on either $\epsilon_{+n,\pm}$ or $\epsilon_{-n,\pm}$. In the strong deflection limit, since higher-order terms decay rapidly, we can only consider the lowest order terms in $\epsilon_{+n,\pm}$ or $\epsilon_{-n,\pm}$ [58] and have

$$\vartheta_{+n,\pm} \Delta\vartheta_S \simeq \theta_\infty \Delta\vartheta_S, \quad (53)$$

$$\vartheta_{-n,\pm} \Delta\vartheta_S \simeq \theta_\infty \Delta\vartheta_S, \quad (54)$$

$$\vartheta_{+n,\pm} \Delta \vartheta_{+n,\pm} \simeq \theta_\infty \Delta \vartheta_0 \epsilon_{+n,\pm}, \quad (55)$$

$$\vartheta_{-n,\pm} \Delta \vartheta_{-n,\pm} \simeq \frac{1}{4} \theta_\infty \Delta \vartheta_0 \epsilon_{-n,\pm}. \quad (56)$$

With above approximations, $\mathcal{V}(u, v)$ can be simplified as

$$\mathcal{V}(u, v) = N(v) \sum_{p=\pm} \sum_{n=1}^{+\infty} (\mathcal{V}_{+n,p} + \mathcal{V}_{-n,p}), \quad (57)$$

where

$$\mathcal{V}_{+n,p} = \epsilon_{+n,p} e^{-2\pi^2 \Delta \vartheta_{+n,p}^2 u^2} e^{-j2\pi p \vartheta_{+n,p} u}, \quad (58)$$

$$\mathcal{V}_{-n,p} = \frac{\epsilon_{-n,p}}{4} e^{-2\pi^2 \Delta \vartheta_{-n,p}^2 u^2} e^{-j2\pi p \vartheta_{-n,p} u}. \quad (59)$$

$N(v)$ follows the definition in Ref. [58] as

$$N(v) = 2\pi I_0 \theta_\infty \Delta \vartheta_0 \Delta \vartheta_S e^{-2\pi^2 \theta_\infty^2 \Delta \vartheta_S^2 v^2}, \quad (60)$$

which contains information about the intensity, location and shape of the source, and is the same for all relativistic images. Normalizing $\mathcal{V}(u, v)$ with respect to $\mathcal{V}(0, v)$, we can remove $N(v)$. The residual is directly related to the properties of each relativistic image. Unless stated otherwise, we will focus on the normalized visibility. The (normalized) overall modulus of $\mathcal{V}(u, v)$ can be obtained from Eq. (57), which contains contributions from the inner and outer relativistic images around the Schwarzschild star. The (normalized) visibility modulus of an individual relativistic image can be derived from Eqs. (58) and (59).

By taking the supermassive compact object M87* as the gravitational lens and considering a spherically symmetric source located at $r_S = 100R_s$ with size $\Delta r_S = 5R_s$, Fig. 3 shows the overall visibility modulus $|\mathcal{V}(u, v)|$ of the inner and outer relativistic images with respect to several values of ϕ_s and ζ . To clarify the contribution from individual relativistic images, we also show the individual visibility modulus $|\mathcal{V}_{\pm n,p}(u, v)|$ of the first- and second-order inner and outer images in the second, fourth and sixth rows. From Fig. 3, we can have three findings. First, the overall $|\mathcal{V}(u, v)|$ of the Schwarzschild star depends on both ζ and ϕ_s , while $|\mathcal{V}(u, v)|$ of the Schwarzschild black hole is only determined by ϕ_s , independent of ζ , since the inner relativistic images depend on $\epsilon_{-n,\pm}$ while the outer ones depend on $\epsilon_{+n,\pm}$. As ζ increases, $|\mathcal{V}(u, v)|$ of the Schwarzschild star gradually approaches that of the Schwarzschild black hole. Second, the structure of $|\mathcal{V}(u, v)|$ for both the Schwarzschild star and the Schwarzschild black hole is staircaselike. However, since the Schwarzschild star has unique inner relativistic images, its $|\mathcal{V}(u, v)|$ gains more steps than the Schwarzschild black hole. More relativistic images also produce more interference, blurring the staircaselike structure of $|\mathcal{V}(u, v)|$ of the

Schwarzschild star. Third, given the length of the baseline, it would be much easier to detect an Schwarzschild star than a Schwarzschild black hole. For the Schwarzschild star, it might be possible to detect the $|\mathcal{V}(u, v)|$ steps generated by the first- and second-order positive-parity inner images by using baselines comparable with the Earth-Moon distance and the Sun-Earth Lagrangian point L2 level, respectively. But for the Schwarzschild black hole [58], baselines with length up to the level of the Sun-Earth Lagrangian point L2 might be required to resolve the $|\mathcal{V}(u, v)|$ step generated by the first-order positive-parity outer image at best. To detect its $|\mathcal{V}(u, v)|$ step generated by the second-order positive-parity outer image, the station needs to be built in the Jupiter orbit [58].

For both the Schwarzschild star and the Schwarzschild black hole, their staircaselike $|\mathcal{V}(u, v)|$ have three characteristics, i.e., the step height, the step width and the interference oscillations in the step, which will be discussed in more detail in the following subsections.

A. Step height

The step height of $|\mathcal{V}(u, v)|$ is an estimator of the observational flux and tells the sensitivity required to observe those images. For the n th-order inner and outer relativistic images, if the baseline is not long enough to distinguish their radial thicknesses, i.e., $\Delta \theta_{\pm n,\pm} u \ll 1$, then $e^{-2\pi^2 \Delta \theta_{\pm n,\pm}^2 u^2} \rightarrow 1$, so that the step height can be approximated by the amplitude of the complex visibility [58]. The heights of the n th-order inner and outer images are respectively

$$h_{-n,\pm} = \frac{1}{4} N(v) \epsilon_{-n,\pm}, \quad (61)$$

$$h_{+n,\pm} = N(v) \epsilon_{+n,\pm}. \quad (62)$$

As shown in Fig. 3, $h_{-n,\pm}$ and $h_{+n,\pm}$ (and their corresponding visibility modulus) are almost constant in this regime.

$h_{-n,\pm}$ depend on both ζ and ϕ_s since they are proportional to $\epsilon_{-n,\pm}$, while $h_{+n,\pm}$ only rely on ϕ_s due to its dependence of $\epsilon_{+n,\pm}$. This suggests that compared with the Schwarzschild black hole, the step heights of relativistic images around the Schwarzschild star have more complicated characteristics.

1. Comparison of step heights between the inner/outer relativistic images

The inner relativistic images directly make the visibility of the Schwarzschild star different from that of the Schwarzschild black hole. Since the step heights of the outer relativistic images can be found in Ref. [58], we focus on the step heights of the inner relativistic images.

According to definitions of $\epsilon_{\pm n,\pm}$ (32) and (44), the step heights $h_{\mp n,\pm}$ decrease as the order n increases, and we have

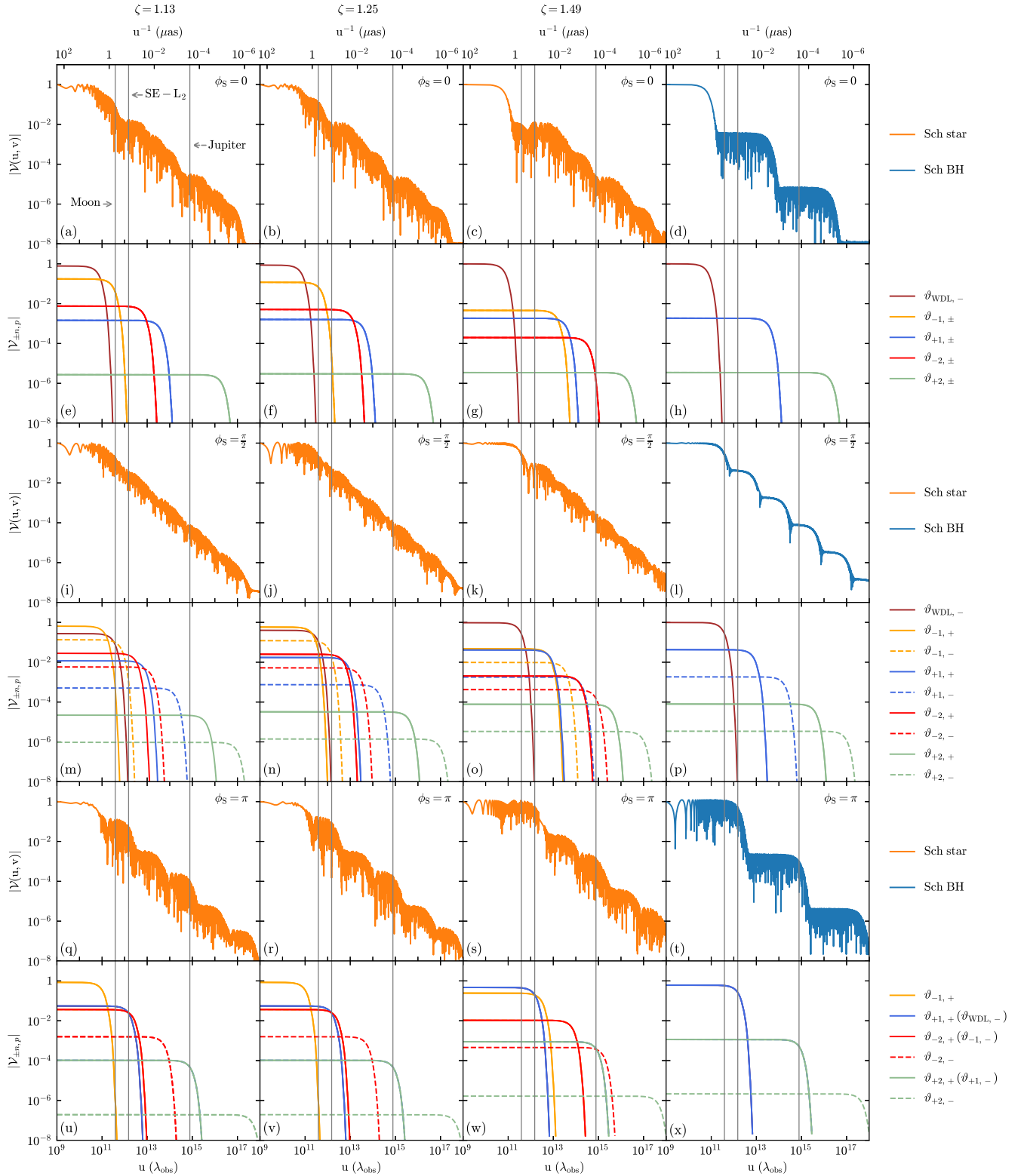


FIG. 3. The normalized visibility modulus $|\mathcal{V}(u, v)|$ of the relativistic images of the Schwarzschild star and the Schwarzschild black hole for several values of the source azimuthal angle ϕ_S and the normalized radius ζ by taking M87* as the gravitational lens. The source distance is $r_S = 100R_s$ with size $\Delta r_S = 5R_s$. The observed wavelength is $\lambda_{\text{obs}} = 1$ mm. The three gray vertical lines represent baselines equal to the distances between Earth and Moon ($u \sim 3.8 \times 10^8$ m), the Sun-Earth Lagrangian point L2 ($u \sim 1.5 \times 10^9$ m) and the Jupiter semimajor axis ($u \sim 7.8 \times 10^{11}$ m), respectively.

$$h_{\mp n,+} \geq h_{\mp n,-} \geq h_{\mp(n+1),+} \geq h_{\mp(n+1),-}. \quad (63)$$

For the inner/outer relativistic images, we find

$$\frac{h_{\mp n,+}}{h_{\mp n,-}} = e^{\frac{2\phi_S}{a_{\mp}}}, \quad (64)$$

and

$$\frac{h_{\mp n,-}}{h_{\mp(n+1),+}} = e^{\frac{2\pi-2\phi_S}{a_{\mp}}}. \quad (65)$$

We can see that due to the relation $\bar{a}_- = 2\bar{a}_+ = 2$, these two ratios depend on ϕ_S only. As shown in Fig. 3, when $\phi_S = 0$, the n th-order positive-parity and negative-parity images have the same step height

$$h_{\mp n,+} = h_{\mp n,-}. \quad (66)$$

When $\phi_S = \pi/2$, we can obtain

$$\frac{h_{\mp n,+}}{h_{\mp n,-}} = \frac{h_{\mp n,-}}{h_{\mp(n+1),+}} = e^{\frac{\pi}{a_{\mp}}}. \quad (67)$$

When $\phi_S = \pi$, the n th-order negative-parity images and the $(n+1)$ th-order positive-parity images have the same step height

$$h_{\mp n,-} = h_{\mp(n+1),+}. \quad (68)$$

With the relation $\bar{a}_- = 2\bar{a}_+$, it is easy to find the relations between the step height ratios of the inner and outer relativistic images as

$$\frac{h_{-n,+}^2}{h_{-n,-}^2} = \frac{h_{+n,+}}{h_{+n,-}}, \quad (69)$$

and

$$\frac{h_{-n,-}^2}{h_{-(n+1),+}^2} = \frac{h_{+n,-}}{h_{+(n+1),+}}. \quad (70)$$

Note that the above discussions are only valid for the comparison between the step heights of the inner/outer relativistic images. It is also necessary to understand the relations of step heights between the inner and outer relativistic images.

2. Comparison of step heights between the inner and outer relativistic images

For the Schwarzschild star, the step height relation among its inner and outer relativistic images varies with ϕ_S and ζ , as shown in Fig. 3. For example, as $\phi_S = 0$ or $\pi/2$, we can find $h_{-1,+} > h_{-2,+} > h_{+1,+}$ for $\zeta = 1.13$ and

1.25, while $h_{-1,+} > h_{+1,+} > h_{-2,+}$ for $\zeta = 1.49$, see Fig. 3 (e–g) and (m–o). However, when ϕ_S increases to π , we have $h_{+1,+} > h_{-2,+}$ for $\zeta = 1.13$ and 1.25 and $h_{+1,+} > h_{-1,+}$ for $\zeta = 1.49$, see Fig. 3 (u–w). There is no strict sequence among the step heights of the inner and outer relativistic images since they are determined by ζ as well as ϕ_S .

In addition to the step height, the step width of $|\mathcal{V}(u, v)|$ is also an observable that is directly related to the baseline length.

B. Step width

As the spatial frequency u increases, the observational resolution gets improved, and the factor $e^{-2\pi^2 \Delta\theta_{\pm n, \pm}^2 u^2}$ in the visibility (57) decreases. When the baseline is long enough to distinguish the radial thicknesses of the relativistic image, i.e., $u^{-1} \sim \Delta\theta_{\pm n, \pm}$, the factor $e^{-2\pi^2 \Delta\theta_{\pm n, \pm}^2 u^2}$ begins to decay rapidly, which results in a drop of $|\mathcal{V}(u, v)|$. When the height of one step is equal to that of the next step, continuing to increase u will reach the next step. In other words, for two adjacent steps, the end point of one step is the starting point of the next step.

For the n th-order relativistic image, we can define the step width $\Delta_{\pm n, \pm}$ as the difference between the end point and the starting point of its $|\mathcal{V}(u, v)|$ step as

$$\Delta_{\pm n, \pm} = u_{\pm n, \pm}^{\text{end}} - u_{\pm n, \pm}^{\text{start}}, \quad (71)$$

which is valid for all $\phi_S \in [0, \pi]$. For the Schwarzschild black hole, according to Ref. [58], we can find

$$\Delta_{+n,+} \leq \Delta_{+n,-} \leq \Delta_{+(n+1),+}. \quad (72)$$

For the Schwarzschild star, the existence of the inner relativistic images has a significant impact on the step width.

In order to clarify the phenomena contained in the step width of the relativistic images around the Schwarzschild star, we select the three highest steps and study their widths. Since the observational resolution is limited by the baseline, these images are more likely to be detected in the future [60].

For the inner and outer relativistic images around the Schwarzschild star, their step widths depend on both ϕ_S and ζ , similar to the step heights, as shown in Fig. 3. For example, when $\phi_S = 0$, the three highest steps come from the relativistic images $\vartheta_{-1, \pm}$, $\vartheta_{-2, \pm}$ and $\vartheta_{+1, \pm}$, and we can find $\Delta_{-1, \pm} < \Delta_{-2, \pm} < \Delta_{+1, \pm}$ for $\zeta = 1.13$ and 1.25, while $\Delta_{+1, \pm} < \Delta_{-2, \pm}$ for $\zeta = 1.49$, see Fig. 3 (e–g). When $\phi_S = \pi/2$, these step widths satisfy $\Delta_{-1,+} < \Delta_{-1,-} < \Delta_{-2,+}$ for $\zeta = 1.13, 1.25$ and 1.49. Besides, we have $\Delta_{-2,+} \approx \Delta_{+1,+}$ for $\zeta = 1.25$ as well as $\Delta_{-1,+} \approx \Delta_{+1,+}$ and $\Delta_{-2,+} \approx \Delta_{+1,-}$ for $\zeta = 1.49$, see Fig. 3 (m–o). Finally, when $\phi_S = \pi$, these widths satisfy $\Delta_{-1,+} < \Delta_{-2,+} < \Delta_{-2,-}$ for $\zeta = 1.13$,

1.25 and 1.49. We have $\Delta_{-2,+} \approx \Delta_{+1,+}$ for $\zeta = 1.13$ and 1.25 as well as $\Delta_{-1,+} \approx \Delta_{+1,+}$ and $\Delta_{-2,-} \approx \Delta_{+2,+}$ for $\zeta = 1.49$, see Fig. 3 (u-w). These results suggest that there is no strict sequence among the step widths of the inner and outer relativistic images. Therefore, under the influence of ζ and ϕ_S , the step widths of all the relativistic images around the Schwarzschild star are more complicated.

C. Interference oscillations in the step

In addition to the heights and widths, the oscillating behavior of the staircaselike $|\mathcal{V}(u, v)|$ is another observable of the relativistic images interferometric signals.

As shown in Fig. 3, $|\mathcal{V}_{\pm n, p}|$ of an individual relativistic image is independent of the phase factor $e^{-j2\pi p \vartheta_{\pm n, p} u}$, see Eq. (57). Thus it behaves as a smooth curve with no oscillations. However, the overall $|\mathcal{V}(u, v)|$ will mix the visibility functions of different relativistic images together, creating additional interference patterns such as $\cos[2\pi u(\vartheta_{+n,+} + \vartheta_{+n,-})]$ to appear in $|\mathcal{V}(u, v)|$, which results in the oscillations shown in Fig. 3.

For the relativistic images around the Schwarzschild black hole, their $|\mathcal{V}(u, v)|$ generally consist of the flat and falling parts, where $|\mathcal{V}(u, v)|$ oscillates with the frequencies $\nu_{+n,+}$ and $\nu_{+n,-}$, respectively [58]. These two frequencies might be extracted if the visibility would be available. It was found that [58]

$$\nu_{+n,+} = \theta_\infty(2 + \epsilon_{+n,+} + \epsilon_{+n,-}), \quad (73)$$

$$\nu_{+n,-} = \theta_\infty(2 + \epsilon_{+n,-} + \epsilon_{+(n+1),+}), \quad (74)$$

and $\nu_{+n,+} > \nu_{+n,-}$. Increasing n reduces the step frequency $\nu_{+n,\pm}$. Based on $\nu_{+n,\pm}$, we can infer the strong deflection coefficient \bar{b}_+ and the apparent radius of the photon sphere θ_∞ for the Schwarzschild black hole [58].

For $|\mathcal{V}(u, v)|$ of the relativistic images around the Schwarzschild star, there are some unique step frequencies, $\nu_{-n,+}$ generated by the interference of $\vartheta_{-n,+}$ and $\vartheta_{-n,-}$, and $\nu_{-n,-}$ generated by the interference of $\vartheta_{-n,-}$ and $\vartheta_{-(n+1),+}$. We find

$$\begin{aligned} \nu_{-n,+} &= \vartheta_{-n,+} + \vartheta_{-n,-} \\ &= \theta_\infty \left(2 - \frac{\epsilon_{-n,+}}{2} - \frac{\epsilon_{-n,-}}{2} \right), \end{aligned} \quad (75)$$

$$\begin{aligned} \nu_{-n,-} &= \vartheta_{-n,-} + \vartheta_{-(n+1),+} \\ &= \theta_\infty \left(2 - \frac{\epsilon_{-n,-}}{2} - \frac{\epsilon_{-(n+1),+}}{2} \right), \end{aligned} \quad (76)$$

and $\nu_{-n,+} < \nu_{+n,+}$. In contrast to $\nu_{+n,\pm}$, decreasing n reduces the step frequency $\nu_{-n,\pm}$. Similar to the step heights and widths, $\nu_{-n,\pm}$ depends on ζ and ϕ_S .

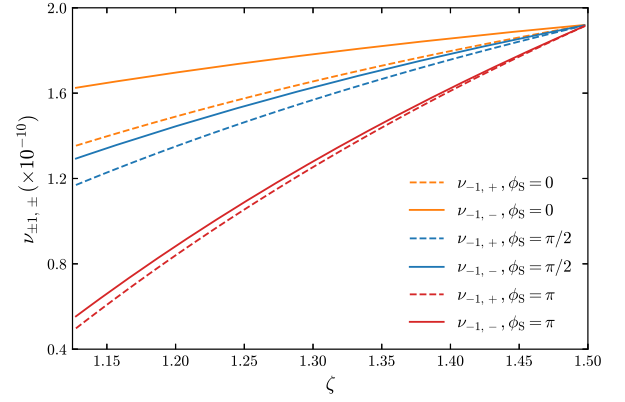


FIG. 4. Setting M87* as a Schwarzschild star and the gravitational lens, the step frequencies $\nu_{-1,\pm}$ with respect to the normalized radius $\zeta \in \mathcal{D}$ for some source azimuthal angle ϕ_S are shown.

Setting M87* as a Schwarzschild star and the gravitational lens, Fig. 4 shows the step frequency $\nu_{-1,\pm}$ with respect to ϕ_S and ζ , where $\zeta \in \mathcal{D}$. It shows that (1) for a given ϕ_S , as ζ increases, $\nu_{-1,+}$ and $\nu_{-1,-}$ increase but the difference between them decreases; (2) for a given ζ , as ϕ_S increases, $\nu_{-1,+}$ and $\nu_{-1,-}$ decrease and the difference between them also reduces.

$|\mathcal{V}(u, v)|$ of the Schwarzschild star has more step frequencies than that of the Schwarzschild black hole. As an example, in Fig. 5(a) we replot $\mathcal{V}(u, v)$ in the range $(1.5 \times 10^{11}, 10^{13})\lambda_{\text{obs}}$ of Fig. 3(b). The flat region I and the falling region II correspond to the visibility modulus

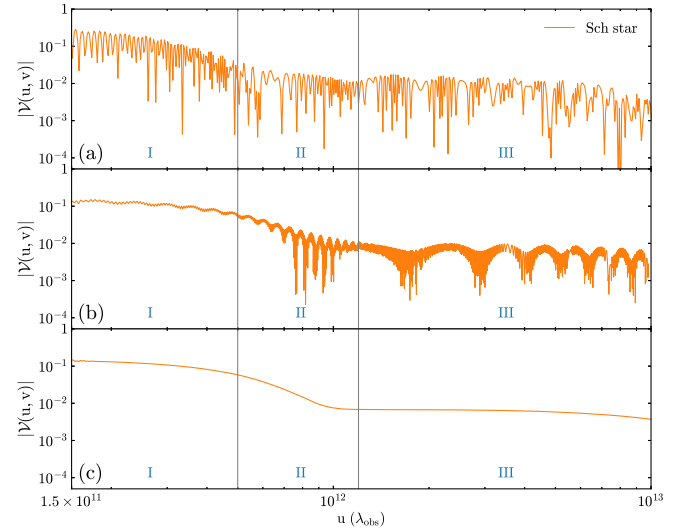


FIG. 5. The visibility modulus of the relativistic images around the Schwarzschild star in the range $u \in (1.5 \times 10^{11}, 10^{13})\lambda_{\text{obs}}$. (a) The original $|\mathcal{V}(u, v)|$ of the first- and second-order positive-parity inner images. (b) $|\mathcal{V}(u, v)|$ after the contributions of $\nu_{-1,+}$ and $\nu_{-2,+}$ are eliminated. (c) $|\mathcal{V}(u, v)|$ after contributions of all the step frequencies generated by the relativistic image interferences are eliminated.

of $\vartheta_{-1,+}$, and the flat region III corresponds to $\vartheta_{-2,+}$. In Fig. 5(b), after subtracting both the interference oscillations of $\vartheta_{-1,+}$ and $\vartheta_{-1,-}$ with frequency $\nu_{-1,+}$ and of $\vartheta_{-2,+}$ and $\vartheta_{-2,-}$ with frequency $\nu_{-2,+}$, we can see that oscillations in regions I and III are significantly suppressed. In Fig. 5(c), we further subtract all other interference oscillations from $\vartheta_{-1,\pm}$, $\vartheta_{-2,\pm}$ and $\vartheta_{+1,\pm}$, making the visibility nearly smooth. It demonstrates that the interference oscillations in the flat regions I and III are dominated by $\nu_{-1,+}$ and $\nu_{-2,+}$, while residual oscillations consists of other step frequencies.

The Schwarzschild star has more complicated step heights, widths and oscillations than those of the Schwarzschild black hole, and observations of its interferometric pattern can in principle be used to infer its strong deflection coefficients and the apparent radius of its photon sphere [58].

V. SPACETIME INFERENCE FROM INTERFEROMETRIC PATTERN

Based on the observational characteristics of the relativistic images' visibility modulus, we might deduce the properties of the lens. For the Schwarzschild black hole, the $|\mathcal{V}(u, v)|$ steps follow a clear height relation and can be easily used to infer its spacetime [58]. Unlike the Schwarzschild black hole, since the inner relativistic images rely on ζ and ϕ_S , it would be more difficult to infer the spacetime of a Schwarzschild star.

Recently, it was found that the relativistic images of a source around the compact object are more visible for $\phi_S = 0$ [58,59]. In this case, the coincidence of the n th-order positive- and negative-parity inner/outer images can simplify the staircaselike structure of the visibility modulus. Besides, as the observational resolution gets improved, the relativistic images with three highest steps are more likely to be resolved in the future [60]. Therefore, we only focus on $|\mathcal{V}(u, v)|$ of these three images with $\phi_S = 0$.

For the Schwarzschild black hole, when $\phi_S = 0$, it was shown that whether the actual measured value of $h_{+1,+}/h_{+2,+}$ deviates from $e^{2\pi}$ can be treated as a criterion for testing the Schwarzschild metric, and using the step frequencies $\nu_{+1,+}$ and $\nu_{+1,-}$, one can obtain \bar{b}_+ and θ_∞ [58].

For the Schwarzschild star, its $|\mathcal{V}(u, v)|$ depends on both inner and outer relativistic images. In the case of $\phi_S = 0$, we find that the relativistic images with three highest steps are always $\vartheta_{-1,\pm}$, $\vartheta_{-2,\pm}$ and $\vartheta_{+1,\pm}$. However, although $h_{-1,\pm} > h_{-2,\pm}$ always holds, the relation among $h_{-1,\pm}$, $h_{-2,\pm}$ and $h_{+1,\pm}$ varies with ζ , see Fig. 3 (e–g). Assuming these images might be practically observed, we must first identify the step heights of $\vartheta_{-1,\pm}$, $\vartheta_{-2,\pm}$ and $\vartheta_{+1,\pm}$, which can be achieved by using the step height ratios.

From the step heights $h_{-1,\pm}$, $h_{-2,\pm}$ and $h_{+1,\pm}$, we notice that the step height ratio $h_{-1,\pm}/h_{-2,\pm}$ has a fixed value independent of ζ , i.e.,

$$\frac{h_{-1,\pm}}{h_{-2,\pm}} = e^{2\pi/\bar{a}_-} = e^\pi. \quad (77)$$

Based on this unique property, we can first identify $h_{-1,\pm}$ and $h_{-2,\pm}$ in the observed three step heights, and further determine $h_{+1,\pm}$. After this, we can extract the oscillations in the flat part of the visibility step to infer \bar{b}_- and θ_∞ .

As discussed in Sec. IV C, it is easiest to extract $\nu_{-1,+}$ and $\nu_{-2,+}$ among all the step frequencies. Using these two step frequencies, we can derive \bar{b}_- and θ_∞ as

$$\sqrt{z_0 z_S} e^{\frac{\bar{b}_- - 2\pi}{\bar{a}_-}} = 2e^{\frac{2\pi}{\bar{a}_-}} (\nu_{-2,+} - \nu_{-1,+}) (\Xi_-)^{-1}, \quad (78)$$

$$\theta_\infty = [2(e^{\frac{2\pi}{\bar{a}_-}} - 1)]^{-1} \Xi_-, \quad (79)$$

where

$$\Xi_- = e^{\frac{2\pi}{\bar{a}_-}} \nu_{-2,+} - \nu_{-1,+}. \quad (80)$$

To measure $\nu_{-1,+}$ and $\nu_{-2,+}$, we need to detect $|\mathcal{V}(u, v)|$ of $\vartheta_{-1,\pm}$ and $\vartheta_{-2,\pm}$, requiring a baseline length equivalent to the Sun-Earth Lagrangian point L2. After \bar{b}_- is known, we will be able to determine ζ from Eq. (41).

Although it is convenient to implement, this method is valid only for $\phi_S = 0$. The general case of $\phi_S \neq 0$ might be our next move.

VI. CONCLUSIONS AND DISCUSSION

In this paper, we investigate the interferometric pattern of the Schwarzschild star in VLBI observations. Taking the finite distance of a source into account, we generalize the strong deflection limit method for an ultracompact object proposed in Ref. [64], and analytically obtain the complex visibility of the inner and outer relativistic images around the Schwarzschild star. We find that like the Schwarzschild black hole [58], the visibility modulus of the relativistic images around the Schwarzschild star also has a staircase-like shape, characterized by the step heights, widths and oscillation frequencies, but is much more complicated. Assuming that the source, the gravitational lens and the observer are perfectly aligned, we also present a preliminary approach to infer the strong deflection coefficients and the apparent radius of the photon sphere of the Schwarzschild star from the interferometric pattern.

To make the Schwarzschild star a black hole mimicker but with distinguishable features, we have assumed that the Schwarzschild star has an electromagnetically transparent surface and relatively high absorption rate in its interior. This configuration can in principle generate an image of a circular ring with an interior brightness depression, satisfying the observational constraints on M87* and Sgr A* at the present stage [12,18]. However, what kinds of matter can realize such a configuration is still unknown to our knowledge, calling for further study.

We do not consider the spin of a Schwarzschild star in this work. The slowly rotating Schwarzschild star [26] and some Kerr interior solutions [78–81] were known. However, the spin effect on the shadow circularity is demonstrated to be small [82], thus we expect that those rotating alternatives are not significantly different from their spherically symmetric counterparts. On the other hand, to date there is still no completely analytical method to describe the relativistic images of a rotating ultracompact object. Together with the work on the analytical analysis for Kerr black hole lensing [83], our results may provide some preliminary understandings about the interferometric pattern of a rotating ultracompact object.

As another important case that this work does not cover, photons might be initially emitted in the radially outward direction inside the photon sphere of an accreting compact object, and they might also be highly lensed, forming the relativistic images [67–69,75]. Their interferometric pattern is still unknown and deserves future work.

In practice, due to the presence of the unique inner relativistic images, the staircaselike structure in the interferometric pattern of relativistic images in the Schwarzschild star spacetime might be less obvious. Its step heights and oscillation frequencies are affected by the source azimuthal angle and the normalized radius of the Schwarzschild star. Therefore, to ensure the accuracy and reliability of the results from observations, it is necessary to develop sophisticated techniques for statistical inference.

ACKNOWLEDGMENTS

This work is funded by the National Natural Science Foundation of China (Grants No. 12273116 and No. 62394351), the science research grants from the China Manned Space Project (Grants No. CMS-CSST-2021-A12 and No. CMS-CSST-2021-B10) and the Opening Project of National Key Laboratory of Aerospace Flight Dynamics of China (Grant No. KGJ6142210220201).

APPENDIX A: PHOTON SPHERE AND ANTIPHOTON SPHERE OF THE SCHWARZSCHILD STAR SPACETIME

From the circular-orbit conditions of a photon that $\dot{r} = 0$ and $\ddot{r} = 0$, we can have $V'_{\text{eff}}(r) = 0$, which gives

$$\frac{A'(r)C(r) - A(r)C'(r)}{C^2(r)} = 0. \quad (\text{A1})$$

For the Schwarzschild star (1), it may have some distinct roots that

- (i) When $r \geq R$, Eq. (A1) reduces to

$$\frac{2r - 3R_s}{r(r - R_s)} = 0, \quad (\text{A2})$$

which has only one real root

$$r_m = \frac{3}{2}R_s. \quad (\text{A3})$$

It can be confirmed that $V'_{\text{eff}}(r_m) = 0$ and $V''_{\text{eff}}(r_m) < 0$, thus $r = r_m$ is the unstable circular orbit of a photon and is defined as the photon sphere. Note that $V''_{\text{eff}}(r_m) < 0$ holds only if $\zeta < 1.5$.

- (ii) When $r < R$, Eq. (A1) leads to

$$9H^2R^2 + 3\sqrt{\frac{\mathcal{H}_R}{\mathcal{H}_r}} + 3\sqrt{\mathcal{H}_R\mathcal{H}_r} = 10, \quad (\text{A4})$$

with \mathcal{H}_R and \mathcal{H}_r given by Eqs. (5) and (6). We can find

$$r_a = 3\zeta\sqrt{1 - \frac{8}{9}\zeta}R_s \quad (\text{A5})$$

for the supercompact Schwarzschild star with $\zeta < \zeta_B$, and

$$r_a = \frac{\zeta^{3/2}}{3}\sqrt{\frac{8\zeta - 9}{\zeta - 1}}R_s \quad (\text{A6})$$

for the Schwarzschild star with $\zeta > \zeta_B$.

From Fig. 6, we know that $V''_{\text{eff}}(r_a) > 0$ for $1 < \zeta < 1.5$, thus the circular orbit at $r = r_a$ is stable and defined as the antiphoton sphere.

We also find that the radius of the antiphoton sphere (A5) for the supercompact Schwarzschild star is just R_0 (10). Photons are forbidden to enter the region of $r \leq R_0 = r_a$. Therefore, we focus on the Schwarzschild star with $\zeta \in (\zeta_B, 1.5)$ only.

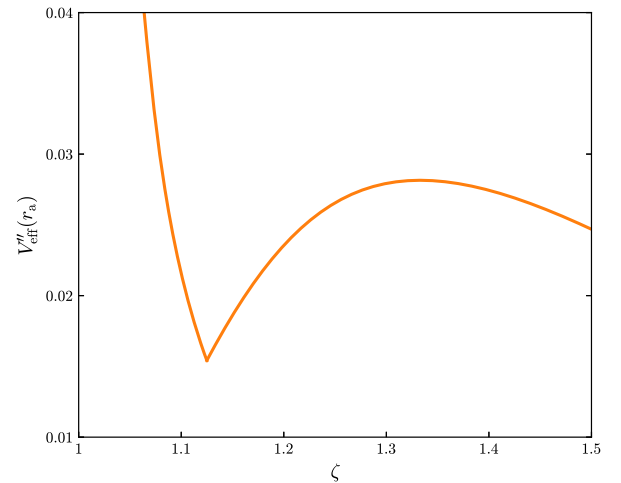


FIG. 6. The second derivative of the effective potential V''_{eff} evaluated at $r = r_a$ with respect to ζ after setting $M = 1$.

The presence of the antiphoton sphere results in the occurrence of r_c , satisfying Eq. (21). We find

$$r_c = -\frac{3\sqrt{3}\zeta}{16\zeta^3 + 27} Q(\zeta)R_s, \quad \text{for } \zeta < \frac{9}{8}, \quad (\text{A7a})$$

$$r_c = \frac{3\sqrt{3}\zeta}{16\zeta^3 + 27} Q(\zeta)R_s, \quad \text{for } \zeta > \frac{9}{8}, \quad (\text{A7b})$$

where $Q(\zeta)$ is given by Eq. (23). In the parameter space $\zeta \in (\zeta_B, 1.5)$, Eq. (A7b) is adopted.

APPENDIX B: DERIVATION OF THE FORMULA (38)

We begin with the variable z from the definition (28) and rewrite the expression for the change in the azimuthal angle (24) as

$$\Delta\phi = \sum_{i=S,O} \int_{1-\frac{r_m}{r_0}}^{z_i} \frac{r_m}{\sqrt{G(z, r_0)}} dz, \quad (\text{B1})$$

where

$$G(z, r_0) = (1-z)^4 \sqrt{\frac{C(z)}{B(z)} \left[\frac{A_0 C(z)}{C_0 A(z)} - 1 \right]}. \quad (\text{B2})$$

For a small z , we can further expand $G(z, r_0)$ as

$$G(z, r_0) \sim \gamma + \delta z + \eta z^2, \quad (\text{B3})$$

where

$$\gamma = \frac{C_m}{B_m} \left(\frac{A_0 C_m}{C_0 A_m} - 1 \right), \quad (\text{B4})$$

$$\delta = \gamma \left[r_m \left(\frac{C'_m}{C_m} - \frac{B'_m}{B_m} \right) - 4 \right], \quad (\text{B5})$$

$$\begin{aligned} \eta = & \gamma \left[-r_m \left(3 + \frac{B'_m r_m}{B_m} \right) \left(\frac{C'_m}{C_m} - \frac{B'_m}{B_m} \right) \right. \\ & \left. + \frac{r_m^2}{2} \left(\frac{C''_m}{C_m} - \frac{B''_m}{B_m} \right) + 6 \right] \\ & + \frac{r_m^2 C_m A_0 C_m}{2 B_m C_0 A_m} \left(\frac{C''_m}{C_m} - \frac{A''_m}{A_m} \right). \end{aligned} \quad (\text{B6})$$

In the limit $r_0 \rightarrow r_c^-$, we find

$$\gamma \rightarrow 0, \quad (\text{B7})$$

$$\delta \rightarrow 0, \quad (\text{B8})$$

$$\eta \rightarrow \eta_m, \quad (\text{B9})$$

where

$$\eta_m = \frac{r_m^2 C_m}{2 B_m} \left(\frac{C''_m}{C_m} - \frac{A''_m}{A_m} \right). \quad (\text{B10})$$

The behaviors of γ , δ and η indicate $G(z, r_c^-) \sim \eta_m z^2$ and thus the integrand in Eq. (B1) is proportional to z^{-1} , which causes $\Delta\phi$ to diverge logarithmically at $r_0 \rightarrow r_c^-$.

In order to isolate this logarithmic divergence, we can split $\Delta\phi$ into a divergent part I_D and a regular part I_R that

$$\Delta\phi = I_D + I_R, \quad (\text{B11})$$

with

$$I_D = \sum_{i=S,O} \int_{1-\frac{r_m}{r_0}}^{z_i} \frac{r_m}{\sqrt{\gamma + \delta z + \eta z^2}} dz, \quad (\text{B12})$$

$$I_R = \sum_{i=S,O} \int_{1-\frac{r_m}{r_0}}^{z_i} \left[\frac{r_m}{\sqrt{G(z, r_0)}} - \frac{r_m}{\sqrt{\gamma + \delta z + \eta z^2}} \right] dz. \quad (\text{B13})$$

After direct integration, I_D becomes

$$I_D = \sum_{i=S,O} \frac{r_m}{\sqrt{\eta}} \log \left(\delta + 2\eta z + 2\sqrt{\eta} \sqrt{\gamma + \delta z + \eta z^2} \right) \Big|_{1-\frac{r_m}{r_0}}^{z_i}. \quad (\text{B14})$$

In the limit $r_0 \rightarrow r_c^-$, it can be expanded by treating γ and δ as small parameters as

$$\begin{aligned} I_D = & \frac{2r_m}{\sqrt{\eta_m}} \log \left[\frac{4\eta_m \sqrt{z_0 z_S}}{\gamma} \left(\frac{r_m}{r_0} - 1 \right) \right] \\ & + \mathcal{O} \left[\left(\frac{A_0 C_m}{C_0 A_m} - 1 \right) \log \left(\frac{A_0 C_m}{C_0 A_m} - 1 \right) \right]. \end{aligned} \quad (\text{B15})$$

According to the definition of γ (B4), we can have

$$\gamma = \frac{C_m}{B_m} \left(\frac{A'_c}{A_c} - \frac{C'_c}{C_c} \right) (r_0 - r_c) + \mathcal{O}(r_0 - r_c)^2, \quad (\text{B16})$$

where the subscript ‘‘c’’ represents quantities evaluated at $r = r_c$. Plugging it into Eq. (B15), we can obtain

$$\begin{aligned} I_D = & -\frac{2r_m}{\sqrt{\eta_m}} \log \left(\frac{r_c - r_0}{\sqrt{z_0 z_S}} \right) \\ & + \frac{2r_m}{\sqrt{\eta_m}} \log \left[4\eta_m \frac{B_m}{C_m} \left(\frac{r_m}{r_c} - 1 \right) \left(\frac{C'_c}{C_c} - \frac{A'_c}{A_c} \right)^{-1} \right] \\ & + \mathcal{O}[(r_c - r_0) \log(r_c - r_0)]. \end{aligned} \quad (\text{B17})$$

With the relation given by Eqs. (B4) and (B16) that

$$r_0 = r_c - \left(\frac{C'_c}{C_c} - \frac{A'_c}{A_c} \right)^{-1} \left(\frac{u_m^2}{u^2} - 1 \right), \quad (\text{B18})$$

we can connect I_D in terms of the impact parameter u as

$$\begin{aligned} I_D = & -\frac{2r_m}{\sqrt{\eta_m}} \log \left(\frac{u_m^2/u^2 - 1}{\sqrt{z_0 z_S}} \right) \\ & + \frac{2r_m}{\sqrt{\eta_m}} \log \left[4\eta_m \frac{B_m}{C_m} \left(\frac{r_m}{r_c} - 1 \right) \right] \\ & + \mathcal{O}[(u_m^2 - u^2) \log(u_m^2 - u^2)]. \end{aligned} \quad (\text{B19})$$

For the regular part I_R , we have

$$I_R = I_R(r_c) + \mathcal{O}[(u_m^2 - u^2) \log(u_m^2 - u^2)], \quad (\text{B20})$$

where

$$I_R(r_c) = \sum_{i=S,O} \int_{1-\frac{r_m}{r_c}}^{z_i} \left[\frac{r_m}{\sqrt{G(z, r_c)}} - \frac{r_m}{\sqrt{\eta_m}|z|} \right] dz. \quad (\text{B21})$$

Bringing all things together, we can finally obtain Eq. (38).

-
- [1] B. P. Abbott *et al.* (LIGO Scientific and Virgo Collaborations), *Phys. Rev. Lett.* **116**, 061102 (2016).
- [2] B. P. Abbott *et al.* (LIGO Scientific and Virgo Collaborations), *Phys. Rev. X* **6**, 041015 (2016).
- [3] B. P. Abbott *et al.* (LIGO Scientific and Virgo Collaborations), *Phys. Rev. Lett.* **116**, 241103 (2016).
- [4] B. P. Abbott *et al.* (LIGO Scientific and Virgo Collaborations), *Phys. Rev. Lett.* **118**, 221101 (2017).
- [5] B. P. Abbott *et al.* (LIGO Scientific and Virgo Collaborations), *Astrophys. J. Lett.* **851**, L35 (2017).
- [6] B. P. Abbott *et al.* (LIGO Scientific and Virgo Collaborations), *Phys. Rev. Lett.* **119**, 141101 (2017).
- [7] K. Akiyama *et al.* (Event Horizon Telescope Collaboration), *Astrophys. J. Lett.* **875**, L1 (2019).
- [8] K. Akiyama *et al.* (Event Horizon Telescope Collaboration), *Astrophys. J. Lett.* **875**, L2 (2019).
- [9] K. Akiyama *et al.* (Event Horizon Telescope Collaboration), *Astrophys. J. Lett.* **875**, L3 (2019).
- [10] K. Akiyama *et al.* (Event Horizon Telescope Collaboration), *Astrophys. J. Lett.* **875**, L4 (2019).
- [11] K. Akiyama *et al.* (Event Horizon Telescope Collaboration), *Astrophys. J. Lett.* **875**, L5 (2019).
- [12] K. Akiyama *et al.* (Event Horizon Telescope Collaboration), *Astrophys. J. Lett.* **875**, L6 (2019).
- [13] K. Akiyama *et al.* (Event Horizon Telescope Collaboration), *Astrophys. J. Lett.* **930**, L12 (2022).
- [14] K. Akiyama *et al.* (Event Horizon Telescope Collaboration), *Astrophys. J. Lett.* **930**, L13 (2022).
- [15] K. Akiyama *et al.* (Event Horizon Telescope Collaboration), *Astrophys. J. Lett.* **930**, L14 (2022).
- [16] K. Akiyama *et al.* (Event Horizon Telescope Collaboration), *Astrophys. J. Lett.* **930**, L15 (2022).
- [17] K. Akiyama *et al.* (Event Horizon Telescope Collaboration), *Astrophys. J. Lett.* **930**, L16 (2022).
- [18] K. Akiyama *et al.* (Event Horizon Telescope Collaboration), *Astrophys. J. Lett.* **930**, L17 (2022).
- [19] S. W. Hawking, *Commun. Math. Phys.* **43**, 199 (1975); **46**, 206(E) (1976).
- [20] S. D. Mathur, *Classical Quantum Gravity* **26**, 224001 (2009).
- [21] V. Cardoso and P. Pani, *Living Rev. Relativity* **22**, 4 (2019).
- [22] K. Schwarzschild, *Sitzungsber. Preuss. Akad. Wiss. Berlin (Math. Phys.)* **1916**, 424 (1916).
- [23] R. M. Wald, *General Relativity* (University of Chicago Press, Chicago, 1984).
- [24] H. Stephani, D. Kramer, M. MacCallum, C. Hoenselaers, and E. Herlt, *Exact Solutions of Einstein's Field Equations* (Cambridge University Press, Cambridge, 2009).
- [25] P. O. Mazur and E. Mottola, *Classical Quantum Gravity* **32**, 215024 (2015).
- [26] C. Posada, *Mon. Not. R. Astron. Soc.* **468**, 2128 (2017).
- [27] C. Posada and C. Chirenti, *Classical Quantum Gravity* **36**, 065004 (2019).
- [28] H. A. Buchdahl, *Phys. Rev.* **116**, 1027 (1959).
- [29] L. Gabbanelli, J. Ovalle, A. Sotomayor, Z. Stuchlík, and R. Casadio, *Eur. Phys. J. C* **79**, 486 (2019).
- [30] J. Ovalle, C. Posada, and Z. Stuchlík, *Classical Quantum Gravity* **36**, 205010 (2019).
- [31] P. Beltracchi and P. Gondolo, *Phys. Rev. D* **99**, 084021 (2019).
- [32] P. O. Mazur and E. Mottola, *Universe* **9**, 88 (2023).
- [33] P. O. Mazur and E. Mottola, *Proc. Natl. Acad. Sci. U.S.A.* **101**, 9545 (2004).
- [34] C. Chirenti, C. Posada, and V. Guedes, *Classical Quantum Gravity* **37**, 195017 (2020).
- [35] R. A. Konoplya, C. Posada, Z. Stuchlík, and A. Zhidenko, *Phys. Rev. D* **100**, 044027 (2019).
- [36] V. Cardoso and P. Pani, *Nat. Astron.* **1**, 586 (2017).
- [37] V. Bozza, *Gen. Relativ. Gravit.* **42**, 2269 (2010).
- [38] S.-S. Zhao and Y. Xie, *J. Cosmol. Astropart. Phys.* **07** (2016) 007.
- [39] X. Lu, F.-W. Yang, and Y. Xie, *Eur. Phys. J. C* **76**, 357 (2016).
- [40] S.-S. Zhao and Y. Xie, *Eur. Phys. J. C* **77**, 272 (2017).
- [41] S.-S. Zhao and Y. Xie, *Phys. Lett. B* **774**, 357 (2017).
- [42] P. V. P. Cunha and C. A. R. Herdeiro, *Gen. Relativ. Gravit.* **50**, 42 (2018).
- [43] X. Lu and Y. Xie, *Eur. Phys. J. C* **79**, 1016 (2019).
- [44] C.-Y. Wang, Y.-F. Shen, and Y. Xie, *J. Cosmol. Astropart. Phys.* **04** (2019) 022.
- [45] F.-Y. Liu, Y.-F. Mai, W.-Y. Wu, and Y. Xie, *Phys. Lett. B* **795**, 475 (2019).

- [46] X. Lu and Y. Xie, *Mod. Phys. Lett. A* **34**, 1950152 (2019).
- [47] X. Lu and Y. Xie, *Eur. Phys. J. C* **80**, 625 (2020).
- [48] Y.-X. Gao and Y. Xie, *Phys. Rev. D* **103**, 043008 (2021).
- [49] X. Lu and Y. Xie, *Eur. Phys. J. C* **81**, 627 (2021).
- [50] Y.-X. Gao and Y. Xie, *Eur. Phys. J. C* **82**, 162 (2022).
- [51] J. Zhang and Y. Xie, *Eur. Phys. J. C* **82**, 471 (2022).
- [52] G. S. Bisnovaty-Kogan and O. Y. Tsupko, *Phys. Rev. D* **105**, 064040 (2022).
- [53] A. Chael, M. D. Johnson, and A. Lupsasca, *Astrophys. J.* **918**, 6 (2021).
- [54] D. C. M. Palumbo and G. N. Wong, *Astrophys. J.* **929**, 49 (2022).
- [55] F. H. Vincent, S. E. Gralla, A. Lupsasca, and M. Wielgus, *Astron. Astrophys.* **667**, A170 (2022).
- [56] H. Pagnat, A. Lupsasca, F. H. Vincent, and M. Wielgus, *Astron. Astrophys.* **668**, A11 (2022).
- [57] S. E. Gralla, D. E. Holz, and R. M. Wald, *Phys. Rev. D* **100**, 024018 (2019).
- [58] F. Aratore and V. Bozza, *J. Cosmol. Astropart. Phys.* **10** (2021) 054.
- [59] O. Y. Tsupko, *Phys. Rev. D* **106**, 064033 (2022).
- [60] M. D. Johnson, A. Lupsasca, A. Strominger, G. N. Wong, S. Hadar, D. Kapec, R. Narayan, A. Chael, C. F. Gammie, P. Galison, D. C. M. Palumbo, S. S. Doeleman, L. Blackburn, M. Wielgus, D. W. Pesce, J. R. Farah, and J. M. Moran, *Sci. Adv.* **6**, eaaz1310 (2020).
- [61] A. Cárdenas-Avendaño and A. Lupsasca, *Phys. Rev. D* **108**, 064043 (2023).
- [62] K. S. Virbhadra and G. F. R. Ellis, *Phys. Rev. D* **62**, 084003 (2000).
- [63] V. Bozza, *Phys. Rev. D* **66**, 103001 (2002).
- [64] R. Shaikh, P. Banerjee, S. Paul, and T. Sarkar, *Phys. Rev. D* **99**, 104040 (2019).
- [65] X.-Y. Zhu and Y. Xie, *Eur. Phys. J. C* **80**, 444 (2020).
- [66] G. N. Wong, *Astrophys. J.* **909**, 217 (2021).
- [67] V. Dokuchaev, *Int. J. Mod. Phys. D* **28**, 1941005 (2019).
- [68] V. I. Dokuchaev and N. O. Nazarova, *Usp. Fiz. Nauk* **190**, 627 (2020).
- [69] P. Kocherlakota, L. Rezzolla, R. Roy, and M. Wielgus, [arXiv:2307.16841](https://arxiv.org/abs/2307.16841).
- [70] P. V. P. Cunha, J. Grover, C. Herdeiro, E. Radu, H. Runarsson, and A. Wittig, *Phys. Rev. D* **94**, 104023 (2016).
- [71] Q. Gan, P. Wang, H. Wu, and H. Yang, *Phys. Rev. D* **104**, 044049 (2021).
- [72] P. V. P. Cunha, E. Berti, and C. A. R. Herdeiro, *Phys. Rev. Lett.* **119**, 251102 (2017).
- [73] M. Guo and S. Gao, *Phys. Rev. D* **103**, 104031 (2021).
- [74] N. Sakai, H. Saida, and T. Tamaki, *Phys. Rev. D* **90**, 104013 (2014).
- [75] V. Bozza and G. Scarpetta, *Phys. Rev. D* **76**, 083008 (2007).
- [76] V. Bozza, F. de Luca, G. Scarpetta, and M. Sereno, *Phys. Rev. D* **72**, 083003 (2005).
- [77] A. R. Thompson, J. M. Moran, and G. W. Swenson, *Interferometry and Synthesis in Radio Astronomy* (Springer, Cham, 2017).
- [78] J. L. Hernandez-Pastora and L. Herrera, *Phys. Rev. D* **95**, 024003 (2017).
- [79] A. P. Ravi and N. Banerjee, *New Astron.* **64**, 31 (2018).
- [80] H. Kim, B. Lee, W. Lee, and Y. Lee, *Phys. Rev. D* **101**, 064067 (2020).
- [81] S. Viaggiu, *Int. J. Mod. Phys. D* **32**, 2350008 (2023).
- [82] D. Psaltis *et al.* (Event Horizon Telescope Collaboration), *Phys. Rev. Lett.* **125**, 141104 (2020).
- [83] S. E. Gralla and A. Lupsasca, *Phys. Rev. D* **101**, 044031 (2020).